communications earth & environment

Article

A Nature Portfolio journal

https://doi.org/10.1038/s43247-026-03983-1

Frictional weakening in the highly mobile 2025 Blatten rock and ice avalanche in Switzerland

Check for updates

Jiahui Kang [1,2] ✉, **Antoine Lucas** [3], **Anne Mangeney** [3,4], **Johan Gaume** [5,6], **Kate Allstadt** [7], **Clément Hibert** [8,9], **Liam Toney** [7], **Hervé Vicari** [5,6], **Michael Dietze** [10], **Mylène Jacquemart** [11,12], **Marc Peruzzetto** [3,13], **Lars Blatny** [6,14], **Michael L. Kyburz** [5,6], **Joachim Rimpot** [8], **Daniel Farinotti** [11,12] & **Fabian Walter** [1] ✉

Cascading slope failures are increasing as glaciers retreat and slopes adjust to a warming climate, yet reconstructing their full dynamics from precursor to deposition remains challenging. Here we show that the 28 May 2025 Blatten rock-ice avalanche, which mobilized about 9.3 million cubic metres, can be reconstructed from seismic, geomorphological, and geotechnical evidence and numerical modeling. The observations reveal the timing, source, volume, and friction of over two weeks of accelerating rockfalls and minor glacier collapses before the main failure, followed by four stages of avalanche motion. Only with drastically reduced friction can both depth-averaged and three-dimensional models reproduce the center-of-mass force history and the deposit distribution. These friction values reflect effective frictional weakening. Geotechnical observations suggest that transient excess pore pressures possibly contributed to this weakening, but are insufficient to rule out additional mechanisms such as ice frictional reduction, segregation, and fragmentation. This work provides a reproducible and robust framework for analyzing catastrophic avalanches under a changing climate.

Cascading mass movements in high mountains are a rapidly growing hazard in a warming climate[1–4]. Cryosphere degradation (glacier retreat, permafrost thaw) and the intensification of hydrometeorological triggers (extreme rainfall, rapid snowmelt) are increasing the frequency and magnitude of these events, creating compounded risks for downstream communities[2,5–8]. From Alaska to the Himalayas, the European Alps, and the Andes, mountains are subject to a new regime of complex, cascading disasters, demanding a renewed focus on the physical processes governing slope failure and runout[8–11].

Progress in understanding such events has advanced on two parallel but often disconnected fronts: pre-failure monitoring for early warning[12–15] and post-event modelling for process understanding and hazard assessment[16,17]. However, quantitative estimates of how the released volume of small precursory events evolves before large mass failure remain elusive. In the meanwhile, numerical models are usually validated only through back-analysis of final deposits[18–20]. This reliance on end-state geometries may fail to capture the dynamics and evolving frictional regimes at play[21].

Seismic observations offer the unique potential to bridge this observational gap. They provide continuous, real-time records of slope activity and capture the forces that moving masses exert on the Earth's surface[22–27]. Comparing these forces with those simulated by granular mass-movement models constrains key event properties such as volume, friction coefficient, and basal conditions[21,28]. For instance, glacier ice within or underneath the moving mass substantially reduces basal friction to enhance mobility[16,21,29]. Different seismic approaches are sensitive to different parts of the failure process. Low-frequency seismic signals are typically applicable only to large

[1]Swiss Federal Institute for Forest, Snow and Landscape Research WSL, Birmensdorf, Switzerland. [2]Faculty of Geosciences and Environment, University of Lausanne, Lausanne, Switzerland. [3]Université Paris Cité, Institut de Physique du Globe de Paris, CNRS, Paris, France. [4]Institut Universitaire de France, Paris, France. [5]WSL Institute for Snow and Avalanche Research SLF, Davos, Switzerland. [6]Institute for Geotechnical Engineering, ETH Zürich, Zürich, Switzerland. [7]U.S. Geological Survey, Geologic Hazards Science Center, Golden, CO, USA. [8]Institut Terre et Environnement de Strasbourg (ITES), Université de Strasbourg, Strasbourg, France. [9]Ecole et Observatoire des Sciences de la Terre (EOST), Université de Strasbourg, Strasbourg, France. [10]Department of Geography, RWTH Aachen University, Aachen, Germany. [11]Laboratory of Hydraulics, Hydrology and Glaciology (VAW), ETH Zürich, Zürich, Switzerland. [12]Swiss Federal Institute for Forest, Snow and Landscape Research WSL, Sion, Switzerland. [13]BRGM, Paris, France. [14]CNRS - UMR 7190, Institut Jean Le Rond d'Alembert, Sorbonne Université, Paris, France. ✉e-mail: jiahui.kang@wsl.ch; fabian.walter@wsl.ch

events via seismic-force inversion[21,22,28], whereas smaller precursor failures can instead be characterized using high-frequency seismic analyses that provide information on event volume and friction coefficient [e.g., refs. 25,30,31]. Despite these advances, studies have rarely integrated pre-failure monitoring, seismic-force inversion of the main event, independent geotechnical or geomorphological constraints, and granular flow modeling within a single framework to analyze the full sequence from precursory activity to catastrophic collapse. Bridging these disciplines could move beyond empirical runout estimates and toward a transferable and robust framework for understanding future cascading disasters.

On 28 May 2025, a rock-ice avalanche with an estimated volume of 9.3×10^6 m^3[32] occurred at Birch Glacier (German: Birchgletscher; Fig. 1a) in Switzerland. The glacier failed under the weight of rock and debris, which had been deposited on its surface after several days of rockfalls from Kleines Nesthorn, located around 600 m above the glacier. The rock-ice avalanche destroyed parts of Blatten, a centuries-old alpine village, and resulted in one fatality.

Here, we combine high and low-frequency seismic records, geomorphological observations, geotechnical data, and granular flow modeling to: (i) track the evolution of failure from the precursory seismic instability (quantifying precursory event volumes and inferring the friction coefficients) to the kinematic evolution of the main collapse (seismic-force inversion), (ii) quantitatively calibrate large-scale rock-ice avalanche runout modeling by optimizing against both seismic-force inversion and high-resolution deposit metrics, and (iii) evaluate plausible frictional weakening processes. We show that drastically reduced friction coefficients are needed to reproduce the observation. Because different processes can produce similar effective friction values, including ice friction reduction, meltwater, and fragmentation, such constraints are inherently non-unique. Geotechnical observations suggest conditions compatible with pore pressure-induced frictional weakening, but cannot rule out other mechanisms. Nevertheless, this exceptionally rich, multidisciplinary dataset establishes a data-constrained benchmark. By delineating what can be explicitly resolved from what remains subject to epistemic uncertainty, this framework provides a robust and transferable way to analyze avalanche dynamics and identify when extreme weakening must have occurred.

Results and discussion

Event records and characteristics

A destabilization sequence lasting more than two weeks preceded the main collapse. Rockfalls from the Kleines Nesthorn onto Birch Glacier intensified on 14 May as reported by the local authority (Fig. 1a). Because these early events were continuously recorded with regional seismic stations, they form a unique, high-resolution dataset for precursory sequence analysis. The increased rockfall activity prompted authorities to evacuate the 300 residents of Blatten as a precaution. The deposition of debris subsequently destabilized the Birch Glacier, leading to accelerated ice flow with velocities of tens of meters per day. On 27 May, an ice avalanche involving several thousands of cubic meters, according to the Lötschental Regional Command Staff[33], detached from the glacier terminus, coming to rest roughly 400 m above the Lonza River flowing along the Lötschental valley bottom (Fig. 1a).

The main collapse on 28 May mobilized ≈ 9.3×10^6 m^3 of material, including ≈ 3.0×10^6 m^3 of ice[32], leaving a head scarp on the Kleines Nesthorn and an adjacent glacier-collapse scarp (Fig. 1b and f). The avalanche mobilized a maximum detachment thickness of 130 m at Kleines Nesthorn and 51 m at the glacier (Fig. 1c–e). Upon detachment, the rock-ice mass descended a narrow gorge (Fig. 1h), traversed the valley bottom and ran more than 200 m up the Weissenried counterslope (Fig. 1g). The final deposits on the valley floor were up to 34 m thick (Fig. 1d and g). The deposit dammed the Lonza River, forming a lake that flooded previously unaffected parts of the village.

The avalanche-generated ground motion was equivalent to an M_L 3.1 earthquake, where M_L is the local magnitude[34]. It generated strong long-period (15–180 s) surface waves that were recorded at distances exceeding hundreds of kilometers (Fig. 1j). Station LAUCH (Fig. 1a) (≈ 5 km away) recorded a signal of around 100 s duration, with an emergent onset and peak ground velocities exceeding 10^{-4} m/s (Fig. 1i).

Precursory destabilization sequence

We used a self-supervised clustering algorithm[35] to quantify the precursory seismic sequence and constrain the nature of the events using continuous vertical-component data from station LAUCH (Fig. 1a) between 1 January and 1 June 2025, segmented into 40,574 180 s time windows. The method identified 236 clusters, 17 of which showed a clear increase in event counts (≈ 700 events, refer to "Methods"). These form two families based on their temporal evolution. Family 1 follows an S-shaped temporal pattern, with activity increasing after 19 May, peaking on 22 May, and then plateauing (e.g., Fig. 2e and g and Supplementary Fig. S2). Family 2 exhibits a gradual increase of event rate from 19 to 28 May (e.g., Fig. 2f and f and Supplementary Fig. S3). Whereas event frequency tracks the progression of instability, the total mobilized mass can evolve independently because the volume of individual events varies[36]. Furthermore, distinguishing the source locations is essential in this complex setting, as failures could originate from either the Kleines Nesthorn or the Birch Glacier.

We used a method[30,31,37] to quantify both the volume and characteristic friction of an event series based on the high-frequency seismic signals coupled with numerical simulations. This is because these small events do not produce low-frequency waves that can be reliably resolved at distant stations. This approach assumes that the scaling relation between radiated seismic energy (E_s) and signal duration (t_s) follows a power law, $E_s = \alpha t_s^{\beta}$. The exponent β serves as a proxy for flow mobility, where higher values indicate stronger energy dissipation and lower mobility (refer to "Methods"). Calculating this relation reveals different behaviors for the observed events: Family 1 shows β = 2.38 ± 0.18, whereas Family 2 gives a lower β = 1.80 ± 0.15 (Fig. 2c, d).

An equivalent power-law relation, $E_p = \alpha' t_p^{\beta'}$, links the loss of potential energy (E_p) to flow duration as shown for lab- and field-scale granular flows[30,37]. To recover these power laws, we performed a series of simulations using the shallow water depth-averaged numerical model (SHALTOP)[38,39], which solves the shallow-flow conservation equations for dense granular flows over complex terrain[17,22,38–43]. To distinguish source locations, we defined two possible source areas: Kleines Nesthorn (Fig. 2a) and the Birch Glacier terminus (Fig. 2b). We simulated 55 events (500–300,000 m^3) at Kleines Nesthorn and 35 events (500–30,000 m^3) at the Birch Glacier terminus, as smaller volumes were reported for the glacier failures.

Assuming that the seismic duration equals the flow duration for each event, we calibrate an energy-conversion ratio $R_{ps} = \frac{E_p}{E_s}$ by matching the duration-energy scaling exponents (β) between observations ($E_s \propto t_s^{\beta}$) and SHALTOP simulations ($E_p \propto t_p^{\beta}$). The β values are then derived from simulations using a constant Coulomb friction rheology with friction angles $\delta \in$ [10°, 20°, 30°] over a range of event volumes and for two source locations. For Kleines Nesthorn, the β values are 2.07 ± 0.24, 2.33 ± 0.20, and 3.01 ± 0.27 (Fig. 2c). For Birch Glacier terminus, they are 1.78 ± 0.15, 2.10 ± 0.19, and 2.46 ± 0.21 (Fig. 2d). Matching the seismic and simulated power laws requires the Kleines Nesthorn source and a friction angle δ = 20° for Family 1. These events are thus most probably rockfalls. In these simulations, the flow typically comes to rest and deposits on the glacier. Family 2 requires a friction angle of δ = 10° and events originating from the glacier terminus, thus corresponding to small rock-ice avalanches. Because SHALTOP computes flow kinematics independent of material mass, its raw output represents kinematic potential energy per unit density. To plot this simulated energy (E_p) in absolute Joules (Fig. 2c, d), we scaled the raw outputs by the mean bulk density of each respective family (refer to "Methods"). Because density acts as a scalar multiplier, this unit conversion has no effect on the calculated scaling exponents (β).

We compared the constant friction results against the empirical volume-dependent law $\mu(V) = \tan\delta = V^{-0.0774}$, which is calibrated for standard dry granular mass movements[42]. For Family 1, our best-fit constant friction δ = 20° matches the $\mu(V)$ equivalent friction angle only at the maximum simulated volume of V = 300,000 m^3

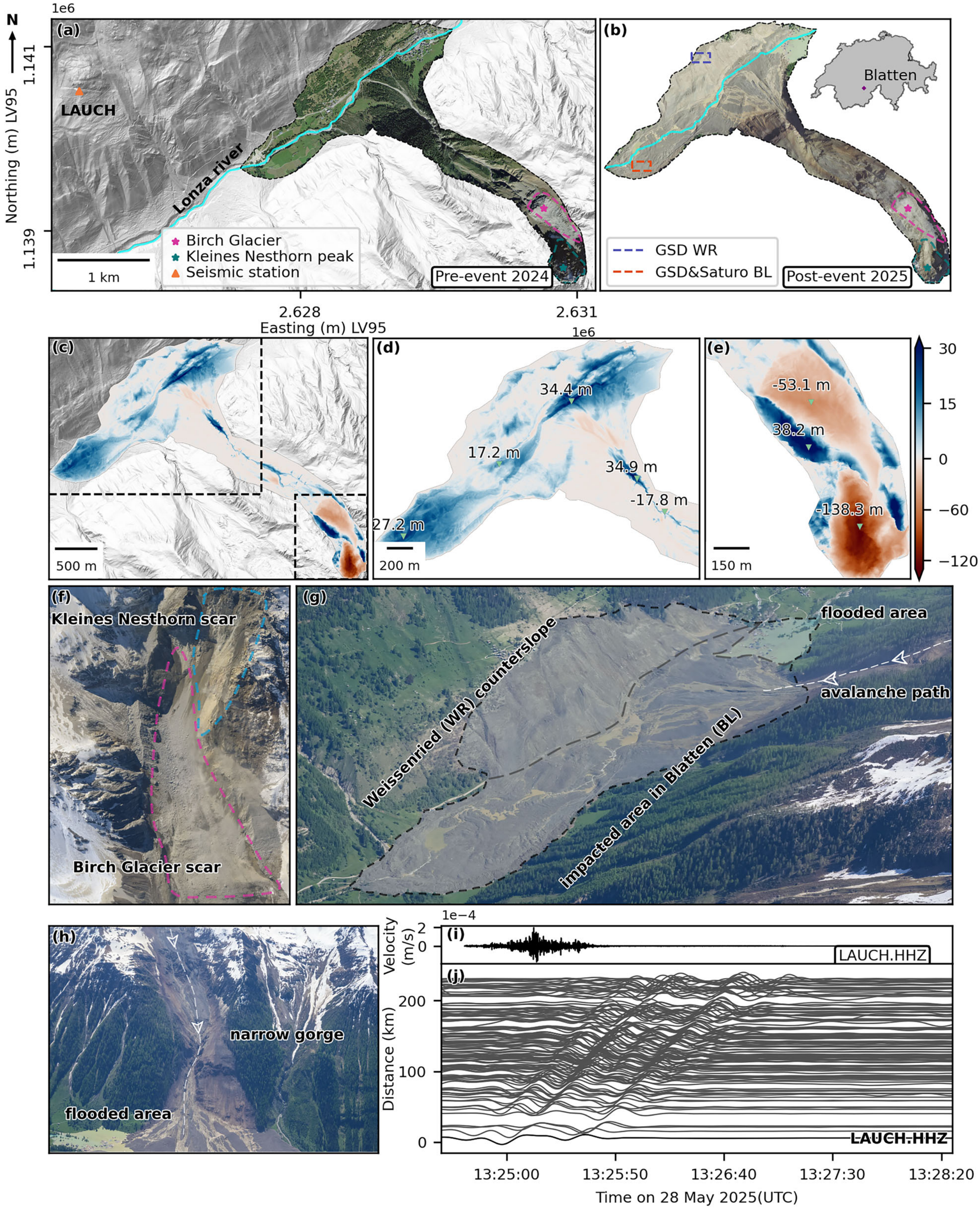

Fig. 1 | Overview of the Blatten rock-ice avalanche. a, b Pre-event (2024) aerial view (SWISSIMAGE 10 cm, 2024[90]) and post-event (30 May, 2025) aerial view[53]. LV95 refers to the official Swiss coordinate reference system (EPSG:2056). Kleines Nesthorn, Birch Glacier, seismic station LAUCH (≈ 5 km away from Birch Glacier), and the Lonza River flowing along the Lötschental valley are indicated. Sampling sites of grain-size distribution (GSD) and SATURO saturated hydraulic conductivity are indicated in (**b**) and described in the "Methods" section. **c–e** Elevation differencing derived from pre- (swissALTI3D, 2024[91]) and post-event (29 May 2025) digital elevation models. **f–h** Field photographs[53]. The photos show the Birch Glacier scar and Kleines Nesthorn scar, the avalanche path with a narrow gorge, the deposition area, and the area flooded by the dammed Lonza River. **i** The vertical-component (HHZ) seismic waveform recorded at LAUCH. **j** Low-frequency (15–180 s) vertical components of seismic signals of the event recorded within 300 km ordered by distance.

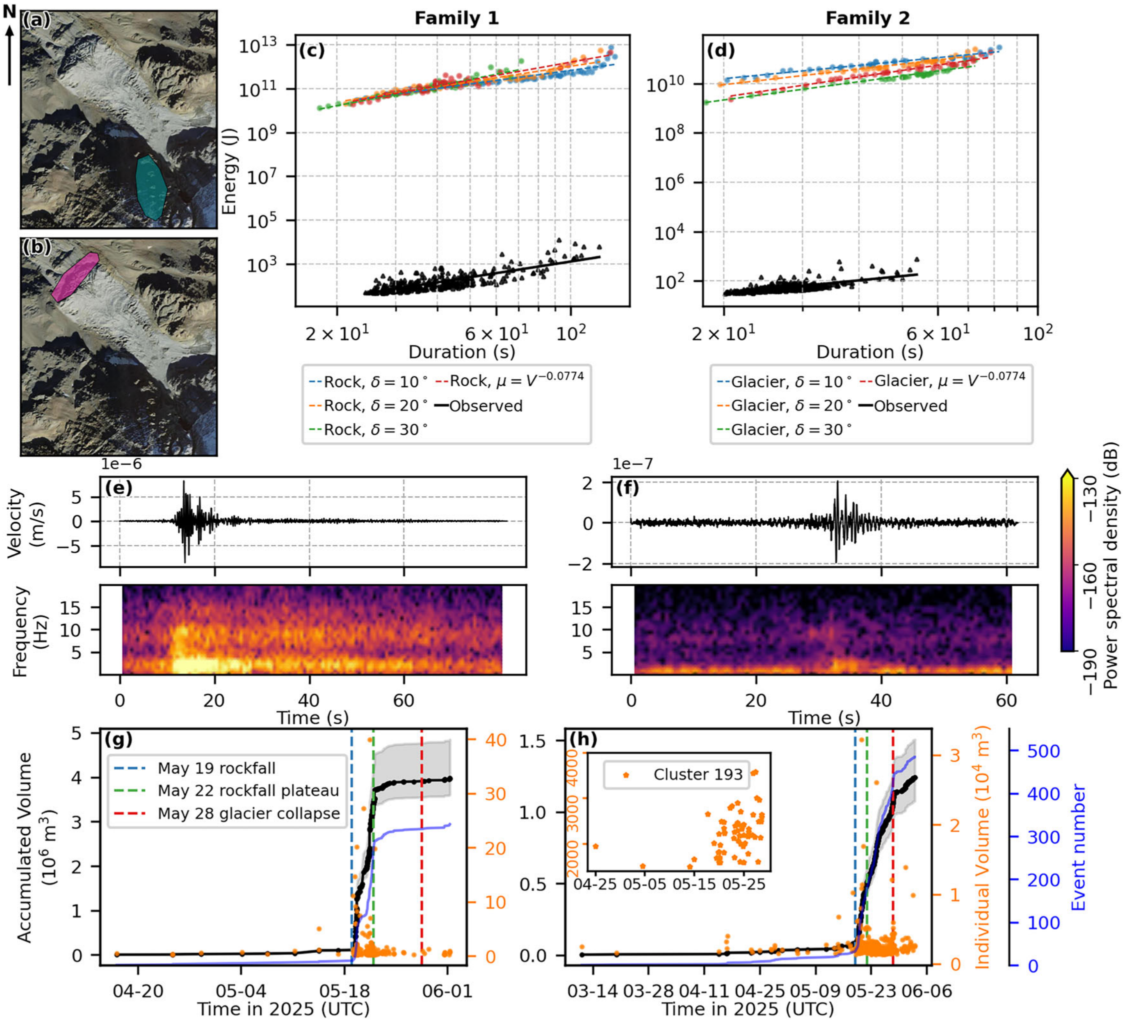

Fig. 2 | Seismic analysis of the precursory destabilization sequence. The left orthophotos (SWISSIMAGE 10 cm, 2024), **a**, **b** show the locations of rockfall (teal) and glacier (pink) sources. **c**, **d** Energy-duration scaling relations used to infer relative mobility for **c** Family 1 (rockfalls depositing on the glacier) and **d** Family 2 (small rock-ice avalanches). Observed seismic events (black triangles) are directly compared to granular flow simulations (colored dashed lines and scatter points). Each color corresponds to a distinct friction angle and each point represents one simulation at a specific volume. **e**, **f** Representative seismic waveforms and spectrograms for Family 1 and Family 2, respectively. **g**, **h** Temporal evolution of the accumulated volume and event number of Family 1 and Family 2. The gray shaded envelopes represent the propagated uncertainty bounds for the volume estimate. Inset of (**h**) highlights cluster 193 with the *y*-axis being the individual volume, showing a clear trend of increasing individual event volume preceding the main collapse.

($\arctan(300,000^{-0.0774}) \approx 20.6°$). This implies that the smaller precursors were more mobile than expected for typical dry granular flows, likely due to pre-existing moisture in the release mass and/or the presence of rainwater as over ≈ 70 mm of rainfall accumulated in May (before 28 May)[44]. Furthermore, for this family, the simulated β exponent predicted by using the $\mu(V)$ law in the simulations across the 500–300,000 m^3 volume range (2.73 ± 0.25) overestimates the observed β (2.38 ± 0.18), which confirms that these events are not dry[31]. For Family 2, the observed β (1.80 ± 0.15) is also substantially smaller than the $\mu(V)$ prediction for its 500–30,000 m^3 volume range (2.71 ± 0.20), requiring a much lower friction angle of 10° as found with the constant Coulomb friction simulations. Recent numerical simulations by ref. 45 demonstrate that adding 70% ice to a granular mixture can reduce its friction angle by half compared to pure rock. Therefore, these Family 2 events are likely small rock-ice avalanches comprised of glacier ice and deposited debris from the slope.

We estimated the individual release volume by linking its radiated seismic energy to the physical loss of potential energy (refer to "Methods"). By accounting for variations in source mass density and energy conversion ratios, we established confidence envelopes for these volume estimates (refer to "Methods"). The cumulative seismic release for Family 1 leads to a cumulative volume reaching 3.91×10^6 m^3 (uncertainty range: 3.54×10^6 to 4.77×10^6 m^3) by 28 May. The S-shaped growth curve indicates rapid mass wasting from the Kleines Nesthorn of 3.75×10^6 m^3 (uncertainty range: 3.40×10^6 to 4.57×10^6 m^3) released by 23 May (Fig. 2g), aligning closely with the 3.50×10^6 m^3 mass loss estimated from digital elevation models (DEM) differencing. The cumulative volume of family 2 grew steadily , reaching 1.09×10^6 m^3 (undertainty range: 0.95×10^6 m^3 to 1.32×10^6 m^3) by 28 May. This estimate represents the total mobilized volume of small rock-ice avalanches, including both glacier ice and previously deposited rock debris. Therefore, the corresponding ice volume was likely substantially smaller, probably on the order of several 10^5 m^3, depending on the rock-ice fraction. Within Family 2, Cluster 193 highlights this trend with increasing individual event volumes preceding the final collapse (Fig. 2h, inset). However, other clusters lack this clear escalation in individual event size, indicating that their cumulative mass wasting volume was primarily driven by event frequency.

Seismic inversion

To resolve the dynamics of the main rock-ice avalanche, we inverted low-frequency (15–180 s) seismic waveforms (Fig. 3a) recorded at distances

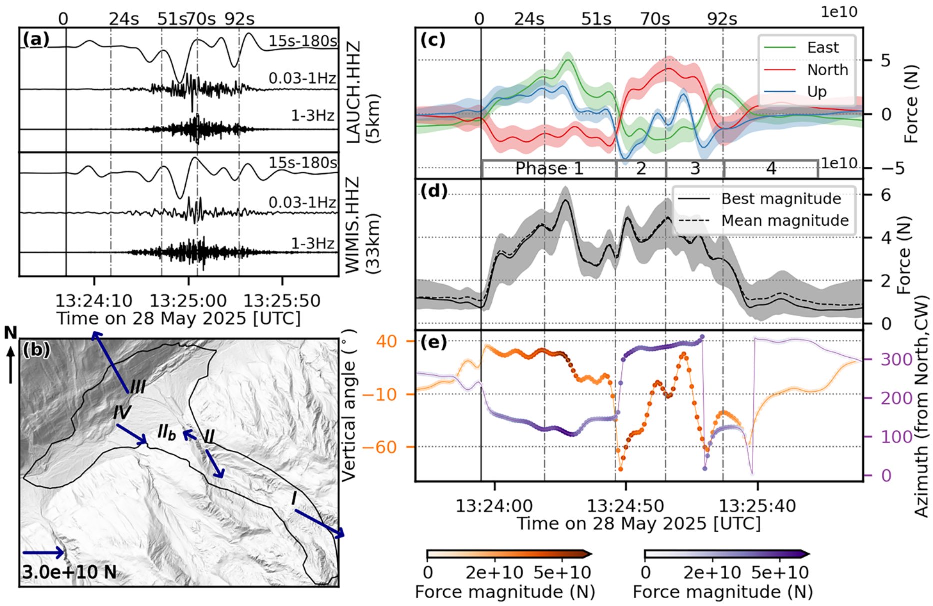

Fig. 3 | Seismic force history of the 28 May 2025 main collapse. **a** Seismic waveforms from two close broadband stations, LAUCH (≈ 5 km) and WIMIS (≈ 33 km), shown in three frequency bands. Roman numerals denote four key kinematic instances discussed in the main text. **b** Shaded relief map (swissALTI3D, 2024) of the avalanche path. The approximately inferred location of the avalanche is shown for each instant with blue arrows indicating the direction and magnitude of the force. **c** Three-component inverted force history. **d** Magnitude of the total inverted force vector. The error bands in (**c**) and (**d**) represent the uncertainty range estimated using a jackknife resampling scheme. The central solid lines in (**c**) and (**d**) denote the "best" inversion, computed using the optimal Tikhonov regularization parameter selected via the L-curve method[46]. The dashed line in (**d**) represents the mean magnitude of the jackknife ensemble. **e** Vertical angle and azimuth of the inverted force vector. The scattered points are color-coded with force magnitude. As the avalanche decelerates and force magnitudes approach zero towards the end of the timeframe, the markers become nearly transparent.

between 33 and 110 km. We used the *lsforce* code[46,47] to estimate the three-dimensional (3D), time-varying equivalent single force exerted on the Earth's surface by the avalanche (Fig. 3c). At long periods, this force is equal to but opposite in direction to the product of the acceleration of the center of mass of the landslide and its total mass[23,24,48].

We interpret four phases in the force history (Fig. 3b–e). During Phase 1 (0–51 s), the mass accelerates as the force magnitude grows steadily, reaching 6×10^{10} N. The force is directed southeast as shown at $t = 24$ s (Fig. 3b and e), opposite, as expected, to the initial acceleration of the mass. Minimal high-frequency (> 1 Hz) energy detected at LAUCH at 5 km distance during this phase indicates limited mass fragmentation[19,27,49,50]. During Phase 2 (51–70 s), the mass transits the gorge and collides with the valley floor. At ≈ 51 s, the force azimuth abruptly rotates by ≈ 180° as the flow enters the narrow gorge. This reversal marks the transition from acceleration (0–*II*) to deceleration (II_b, 54 s) and captures the strong centripetal forces during flow confinement. The first burst of high-frequency energy (> 0.3 Hz) appears at this instant (Fig. 3a), indicating internal collisions of the rock-ice mass. As the avalanche exits the gorge and collides with the Weissenried counterslope (*III*, 70 s), the force reaches 5×10^{10} N and the flow radiates elevated high-frequency seismic energy. Phase 3 (70–92 s) consists of flow redirection and secondary runup. Following the impact of the avalanche with the Weissenried counterslope, the force vector swings southwest during the backflow of material toward Blatten and the lateral spreading of the mass. A secondary force peak near 92 s corresponds to a smaller runup towards the valley side of initial descent and southwestward azimuth change, consistent with observed deposit geometry and high-frequency bursts[25]. Phase 4 (> 92 s) describes the spreading and final mass deposition. The force magnitude decays as the bulk of the rock-ice avalanche comes to rest. High-frequency radiation ceases, indicating that energetic collisions have ended and motion is dominated by the slow spreading of the depositing flow.

Rock-ice avalanche modeling

Whereas most landslide back-analyses rely on one runout model, we used two complementary numerical runout models to test different rheologies to get model-independent insight into the flow properties. SHALTOP provided an efficient framework to explore the rheological parameter space, whereas a Material Point Method (MPM) model[51,52] was used to assess the consistency of the resulting flow kinematics in 3D. The MPM model, which solves the mass and momentum balance equations in an Eulerian-Lagrangian framework and resolves the full 3D stress field, can capture detachment, internal shearing, and curvature effects beyond the reach of depth-averaged models. We modeled the long-period force histories predicted by each model simulation based on the center of mass trajectories.

The granular flow models were constrained with independent observations: (i) mapped deposit distribution and flow-related features from DEM differencing between 23 May and 29 May 2025 and orthophotos[53] (Fig. 4a, b), and (ii) the inverted seismic force history (Fig. 4k). Model performance was evaluated using four control metrics (refer to Supplementary Information S1): (1) spatial overlap of observed deposit outlines and maximum spatial extent of the simulated deposits (Trimline ratio); (2) Root Mean Squared Error of deposit thickness (Thickness RMSE); (3) normalized cross correlation between the simulated and inverted force histories (Cross-corr); and (4) RMSE of simulated versus inverted force amplitudes after aligning for the maximum cross correlation (Amp RMSE). Because these four metrics possess different units and scales, direct arithmetic combination is invalid. To resolve this, we transformed each raw metric into a *z*-score, which quantifies standard deviations from the mean performance across all simulations[54]. We assigned a combined weight of 0.7 to the deposit metrics (Trimline ratio and Thickness RMSE) and 0.3 to the seismic metrics (Cross-corr and Amp RMSE). This uneven weighting is justified for two reasons. First, high-resolution topographic differencing provides direct, low-uncertainty measurements, whereas seismic inversions are indirect calculations with accumulated wave-propagation and point-source uncertainties. Second, seismic force history reflects bulk center-of-mass accelerations that are most sensitive to the highly mobile phases of the event. As the mass loses momentum, the signal-to-noise ratio drops, leaving the late-stage depositional dynamics partially unresolved.

We tested different rheologies that represent distinct assumptions and complexities about frictional behavior: a constant friction Coulomb model, a two-parameter Voellmy model, volume-dependent $\mu(V)$ law and laws with variable friction coefficient: velocity ($\mathbf{u}$)-dependent $\mu(\mathbf{u})$ law, and the $\mu(I)$ rheology, which depends on the inertial number I[55]. The Coulomb model assumes time-invariant basal friction. The Voellmy model adds a velocity-squared turbulent drag term to account for increased resistance at high velocity. $\mu(V)$ assumes friction is constant in time and space but varies with event volume, whereas $\mu(\mathbf{u})$ and $\mu(I)$ permit friction to evolve dynamically with flow velocity or inertial number (refer to Supplementary Information S2). Given its well-established integration with seismic force inversion [e.g., refs. 21,22,26,29], we used SHALTOP to perform the

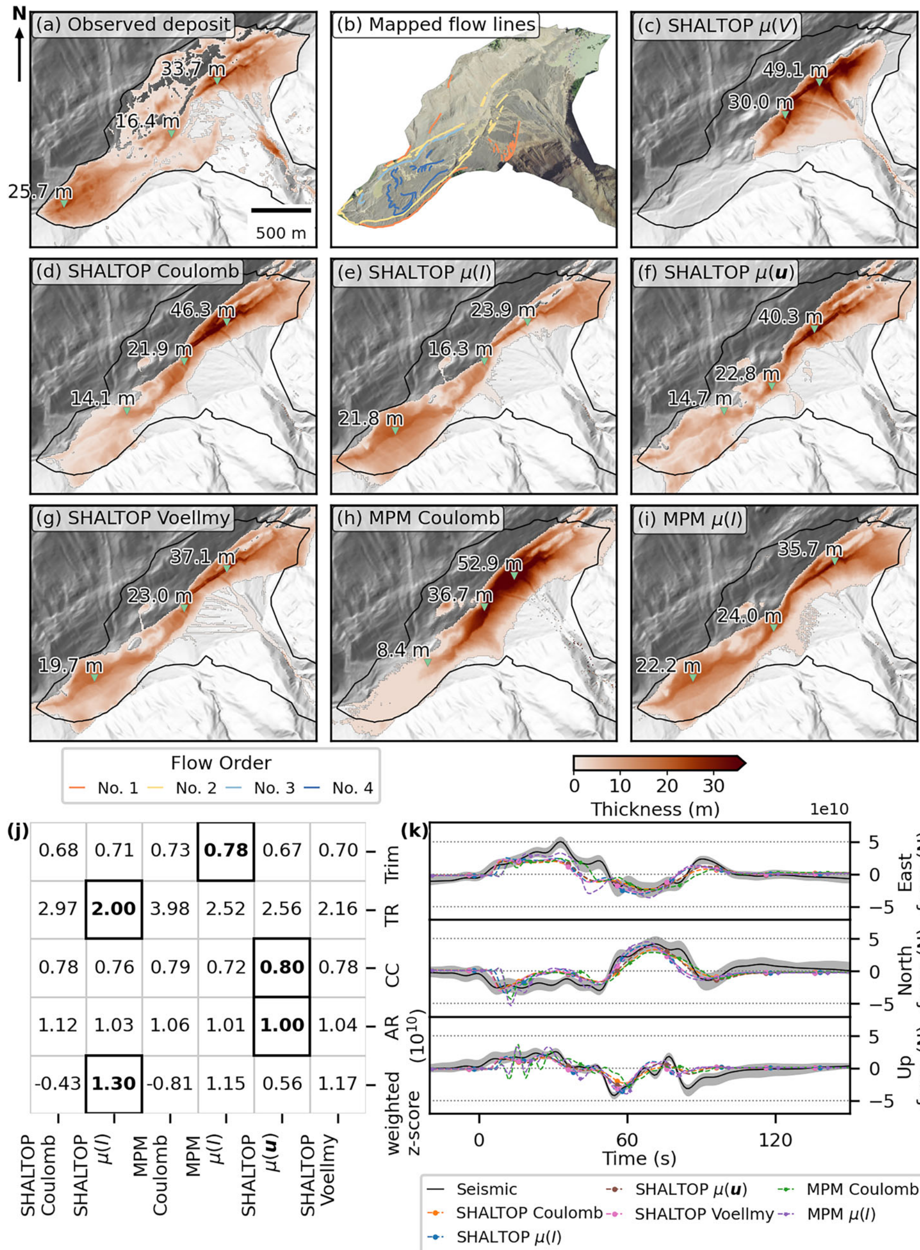

Fig. 4 | Comparison of simulation results with deposit and seismic constraints. **a** Observed final deposit thickness. **b** Mapped flow lines based on geomorphological features from post-event (30 May, 2025) aerial view (data sources as in Fig. 1). Colors indicate relative flow sequence, from early (warm colors) to later (cool colors) stages. **c**–**i** Simulated final deposits from SHALTOP and MPM across different rheologies, each representing the specific simulation that achieved the best overall metric z-scores. Black contours delineate observed deposit outlines. **j** Quantitative comparison of model performance against the final deposit (Trimline ratio (Trim), Thickness RMSE (TR)) and seismic force history (Cross-correlation (CC), Amplitude RMSE (AR)) as well as the weighted *z*-score. The best scores among the simulations are bolded. **k** Comparison between the three components of the inverted seismic force and the forces predicted by each model simulation. The error bands represent the uncertainty range for seismic inversion estimated using a jackknife resampling scheme. The central solid lines in denote the "best" seismic inversion, computed using the optimal Tikhonov regularization parameter selected via the L-curve method[46].

primary sensitivity analysis across the listed basal friction laws. Although fully coupled two-phase thermo-hydro-mechanical models could, in principle, describe pore pressure effects, low ice friction and melt-induced frictional weakening[56–61], these processes, the associated material parameters, and the initial conditions remain difficult to constrain in natural terrain. Therefore, we used the aforementioned one-phase frictional models and treat μ as a parameter that is calibrated to reproduce deposit geometry and seismic data. Because the exceptionally well-documented Blatten event was captured by multiple independent observations, it provides a robust basis for determining the frictional model that best reproduces the data, and constraining its parameters, resolving the flow dynamics. The resulting value of μ reflects effective energy dissipation, with lower μ indicating frictional weakening mechanisms that enhance flow mobility.

When calibrating different models to maximize their fit to the observations, the metrics reveal distinct strengths and limitations across different rheologies (Fig. 4j, refer to Supplementary Data 1 for the full sensitivity analysis). For a release volume of $\approx 9.3 \times 10^6$ m^3, the $\mu(V)$ law, empirically fitted on essentially dry landslides, predicts $\delta \approx 16°$ with confidence intervals from 8° to 20°[42]. However, simulations using these values underestimate the observed runout, indicating that the Blatten event was more mobile than expected for dry landslides of comparable size (Fig. 4c). Although Coulomb rheology with $\delta = 8°$ approximates the distal extent of the deposits (Fig. 4d), it yields the poorest match for the deposit distribution. The $\mu(\mathbf{u})$ rheology achieves the highest performance against the seismic constraints (Fig. 4j, k). However, it fails to accurately distribute the mass and gives a high Thickness RMSE and the lowest Trimline ratio among the available models (Fig. 4f and j). The Voellmy rheology provides an intermediate fit but still underestimates lateral spreading (Fig. 4g and j). Only the $\mu(I)$ parameterization (Fig. 4e) captures the late-stage flow surge that produces the thicker deposit distribution at the southwestern margin, where friction decreases toward its lower bound μ_1 during the depositional stage of the simulation (Supplementary Fig. S4). We then ran the 3D MPM model for Coulomb and $\mu(I)$ to also simulate the depth-resolved flow kinematics (Fig. 4h, i). For the Coulomb model, the best-fit basal friction angle is $\delta = 11.8°$ for the MPM simulation, which is also near the lower bound of empirical estimates for rock-ice avalanches[42,62]. However, similar to the SHALTOP results, this

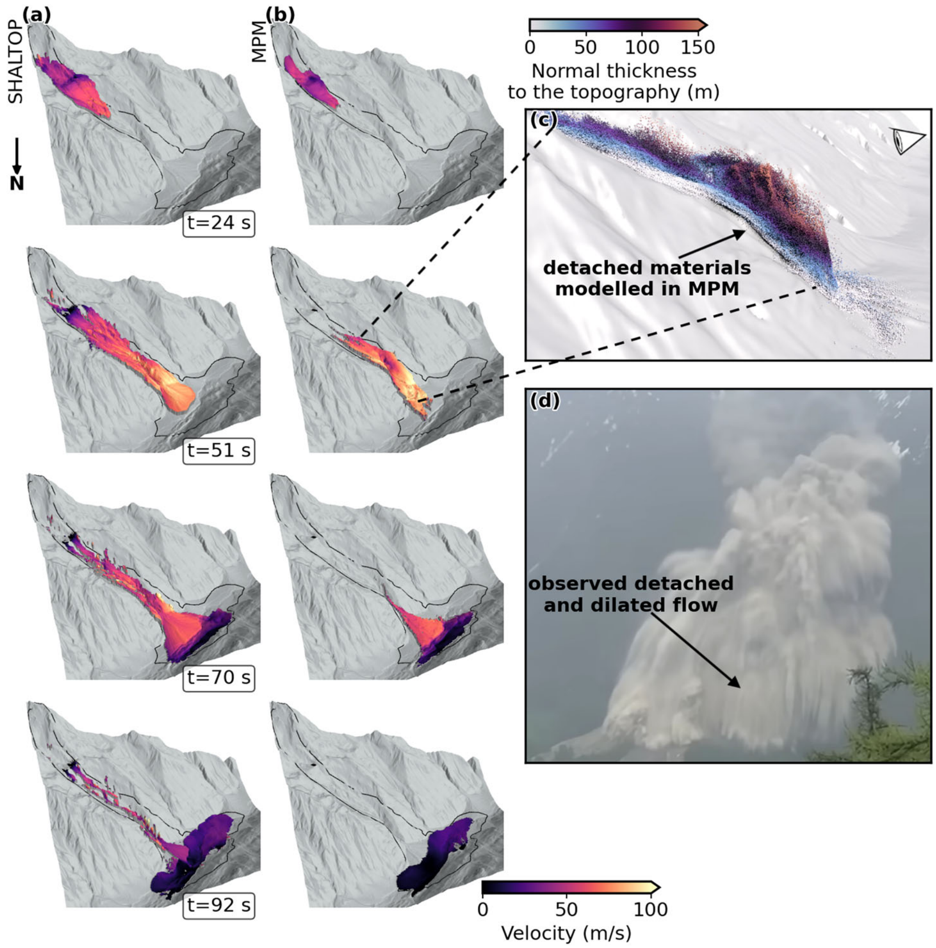

Fig. 5 | Snapshots of simulated avalanche dynamics for the $\mu(I)$ rheology. The panels compare the velocity fields predicted by **a** SHALTOP and **b** MPM at key kinematic instances corresponding to the seismic analysis in Fig. 3: acceleration (*I*, 24 s), gorge transit (*II*, 51 s), valley-floor collision (*III*, 70 s), and flow redirection (*IV*, 92 s). **c** Close-up of the 3D MPM simulation during gorge transit, highlighting detached materials (dashed connectors indicate the view location). The eye symbol marks the approximate viewing direction of the video frame in (**d**). **d** Frame extracted from video (courtesy of the Canton of Valais) showing the observed detached particle cloud at a similar stage of the avalanche.

constant friction fails to reproduce the observed deposit geometry. For the $\mu(I)$ rheology, the bounds $\delta_1 = 2°$ and $\delta_2 = 12°$ were adopted in SHALTOP and $\delta_1 = 1°$ and $\delta_2 = 16°$ for MPM, where δ_1 and δ_2 denote the lower and upper limits of the $\mu(I)$ law. Also in the MPM simulations, the $\mu(I)$ parameterization provides a better reproduction of the observations than a constant Coulomb friction model.

Crosscutting levees and lobes on the deposit allow the reconstruction of at least four flow pulses towards the southwest margin of the deposit. We refer to these pulses as flow order 1–4, defined by their relative timing inferred from crosscutting relationships: earlier deposits are overlain and locally incised by later, channelized surges (Fig. 4b). The first pulse determined the maximum southern extent, running ≈ 80 m (vertical) up in the direction of the source area before flowing farther downstream (flow order 1 in Fig. 4b). Superimposed on this initial deposit are elongated lobes with levees (flow order 2–4 in Fig. 4b) that extend almost 2 km downstream, beyond the village of Blatten. These channelized features incised the initial deposit from the first pulse, indicating a subsequent highly mobile surge. Because a constant-friction rheology fails to capture these complex morphological features, reproducing their extended runout requires the $\mu(I)$ rheology's extreme drop in friction. The near-zero friction required during several critical stages (Supplementary Fig. S4) strongly indicates the material underwent frictional weakening mechanisms. We explicitly state that the friction coefficient represents a calibrated effective bulk value that suffers from equifinality. This equifinality is inherent to the use of one-phase models, in which different physical mechanisms are absorbed into an effective friction term. Beyond ≈ 92 s, the avalanche's center-of-mass decelerates and the remaining motion transitions into slower, lateral spreading, which produces weaker and more complex force signatures. This complex force history evades the seismic constraints as the low-frequency seismic signals are too weak compared to the background noise.

Comparisons at four representative times (24, 51, 70, 92 s) (Fig. 5a, b) show consistent kinematics between SHALTOP and MPM, with MPM additionally resolving the dilated flow detaching from the topography in the narrow gorge (Fig. 5c, d). The flow front impacts the gorge wall, which causes the flow to climb over it. As the valley floor turns concave-downward, the flow partially detaches from the terrain, which is captured explicitly by MPM (Supplementary Video 2). Despite the different model dimensionalities, the velocity magnitudes of SHALTOP and MPM remain in close agreement throughout the phases. The consistency between the $\mu(I)$ simulations for SHALTOP and MPM across independent metrics and their best z-score for each model demonstrates that the observed runout and dynamics are only reproduced when δ_1 is exceptionally low (2°/1°). This indicates that the effective friction varied significantly throughout the flow with persistent frictional weakening.

Mechanisms driving avalanche mobility

One or several frictional weakening mechanisms must have acted to produce the high mobility of the Blatten rock-ice avalanche[42,63,64], extending beyond the physical assumptions of dry granular flows[55]. However, the calibrated friction values obtained from the one-phase models should be interpreted as effective bulk parameters. Here, we therefore evaluate the potential contributions of several weakening mechanisms qualitatively, using field observations, geotechnical measurements, energy-balance estimates, and model-inferred friction patterns as supporting evidence. Their relative contributions cannot be uniquely resolved with the available observations.

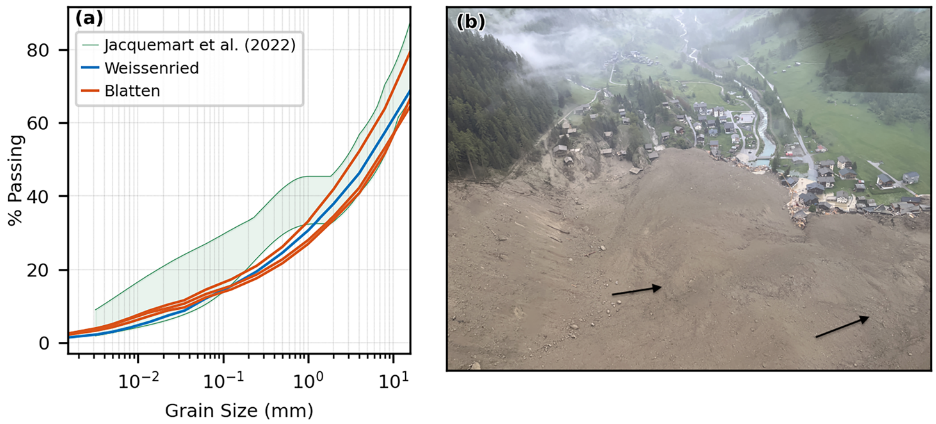

Fig. 6 | Grain-size distributions and field observations of the avalanche deposits. **a** Grain-size distributions of one sample from the Weissenried counterslope (blue) and three samples from the Blatten main deposit (orange). The collected samples included coarse gravel and small cobbles, up to ≈ 5 cm, but excluded larger boulders. The grain-size distribution is compared with data from the Flat Creek glacier detachment deposits reported by ref. 71, rescaled so that the maximum measured grain size corresponds to 5 cm for comparison. **b** Field photograph on 28 May showing the Blatten deposit with darker zones (black arrows) indicating locally wet conditions (ETH Zürich).

A primary factor is rock-ice friction reduction. The Blatten rock-ice avalanche involved a total volume of $\approx 9.3 \times 10^6$ m^3, including $\approx 3.0 \times 10^6$ m^3 of ice. The substantial ice content likely favored low-friction interactions within the mixture[45,65–67]. As demonstrated by ref. 45, an ice fraction of 32% can reduce the bulk friction angle by approximately 20%. This reduction may explain the best-fit constant Coulomb angles (8°/11.8°). However, the deposit is not reproduced with constant Coulomb friction; instead, it requires a variable friction as in the $\mu(I)$ law with extreme frictional drop to near-zero lower bounds (2°/1°). Therefore, ice content alone may not fully explain the large observed mobility.

The strong shearing of the rock-ice debris under high normal stress likely also led to dynamic fragmentation, further amplified by strong impact loading against the steep, irregular topography. The fragmentation process could rapidly produce fine particles within the rock-ice mixture and enhance mobility[68]. As shown in Supplementary Fig. S4, these expectations agree with our low friction modeled with $\mu(I)$ parameterization during failure, gorge transit, and collision with the counterslope (instances *I*, *II*, and *III* in Fig. 3, respectively).

Frictional and impact heating during rapid flow may also have generated meltwater, further reducing basal resistance[62]. Sosio et al.[69] reported calibrated bulk basal friction angles as low as 2.75° for the Sherman ice-rock avalanche with volumes of order 10^7 m^3 that involved 2×10^6 m^3 of ice. Our energy-balance estimate suggests a potential meltwater volume of $\approx 0.88 \times 10^5$ to 2.21×10^5 m^3 (see "Methods"). Together with water present in the release mass (which cannot be quantified from our observations), this meltwater may have increased pore water pressures in parts of the landslide. Elevated pore water pressures can reduce internal and basal shear stresses by lowering effective stresses in the solid phase[58,70].

Field surveys conducted shortly after the event documented wet deposits (Fig. 6b), but the hazard posed by potential secondary landslides prevented direct measurements of water content and liquefaction. Consequently, the possible occurrence of elevated pore water pressures can only be inferred indirectly from geotechnical analyses of the deposited sediments that we collected later. Grain-size analysis of four samples from the counterslope and main deposit (Fig. 6a) reveal a high fine material content (≈ 15% silt and clay), classifying the material as well-graded (poorly sorted) gravel with fines, and consistent with the low permeability measured in the deposits ($k_0 \approx 10^{-12}$ m^2) (refer to "Methods"). These fine particles likely originate from both the rock/debris mass from the Kleines Nesthorn and subglacial till from the Birch Glacier. The sediment's texture closely resembles that of another documented fine-rich rock-ice avalanche at Flat Creek (Alaska)[71], where the high fraction of fines originated from subglacial till. Such fine-grained, low-permeability material can hinder dissipation of high excess pore pressures if these were generated during flow[70]. Impacts with the complex topography induce shearing and compression of the material. These processes may be at the origin of rapid pore pressure generation due to shearing-induced dilatancy effects or isotropic pressurization[56]. Because of the low permeability, these excess pore pressures would have dissipated slowly, allowing frictional weakening to persist[56]. These observations are therefore consistent with conditions that promote fluid-assisted weakening. However, they are not sufficient to determine whether pore pressure effects were dominant, nor to quantify their contribution relative to other processes.

Alternative physics-based multiphase models could provide further insights into the processes responsible for friction reduction, including pore pressure weakening, dynamic fragmentation, rock-ice friction reduction, and meltwater generation[56–61]. However, the accurate description of these processes is still an open issue, and such models require knowledge of parameters that are both highly uncertain and, in some cases, effectively unmeasurable, yet potentially exert a strong influence on the modeled dynamics[56,58,61]. Clear examples include the initial water content, initial dilatancy angle, and permeability evolution during the flow, all of which can substantially affect the magnitude of excess pore pressures generated during motion[61].

Hazard assessment implications

Atmospheric warming and permafrost thaw enhance rockfall activity in high-alpine environments[7,72,73]. Consequently, rocks and debris are more likely to deposit onto or mix with glacier ice, potentially increasing the ice content of catastrophic failures. For the main Blatten rock-ice avalanche, we showed that this effect led to an exceptionally mobile rock-ice avalanche. The presence of ice also led to lower friction for precursory events, which include failures that deposited on the glacier as well as those that originated from it. Granular frictions, typically used to model dry rock avalanches[42] were not sufficiently small to capture the events' mobility.

The integration of oblique aerial photography, geotechnical field characterization of sediments and broadband seismic data is key to constraining and interpreting mobility and, therefore, the hazard potential of rock-ice avalanches. The involvement of glacial ice has been suggested in runout modeling of historic events[16,21,29,74], and the multi-sensing approach of the present study sets a standard approach to systematic determination of effective friction. On the other hand, for hazard management of future events or ongoing mass movement activity resulting from rock instability, our seismic signal classification also provides a useful tool. The unsupervised signal clustering[35], combined with granular flow modelling, can identify telltale event types and quantify volumes associated with slope failures that can be specifically monitored in case other observations are unavailable. In our case, this was possible with an earthquake monitoring seismometer providing real-time mass movement detections at a distance of ≈ 5 km from the Blatten area. As machine learning algorithms continue to enhance seismic signal processing, streaming seismometers will play an increasingly important role in slope monitoring and can provide information on precursory events as soon as an instability is identified. This is already now possible, whereas comprehensive identification of mass movement signals in an entire seismic network may not yet be feasible as a result of limitations in computational power, training data and algorithm transferability. Importantly, in our case, a closer analysis of the precursory rockfall activity already pointed out the need to employ low friction angles and thus expect high mobility of failing masses in the main event.

Ultimately, our results show that both depth-averaged flow models and 3D granular models capture increased runout mobility when forced and interpreted with pivotal data. The combination of state-of-the-art and robust seismology, direct geomorphological observations, geotechnical experiments and granular flow models therefore holds great potential in understanding previous and managing future hazardous mass movements. To support reproducibility and future applications, we also provide an Avalanche Dynamics Analysis Cookbook (ADAC) that documents the modelling and seismic-analysis workflow, links to the underlying open-source tools, and archives the Blatten analysis package (Supplementary Information S4). This framework should be deployed in a systematic campaign analyzing other rock-ice avalanches. By expanding this dataset, the scientific community could derive robust empirical laws that are similar to those established for dry flows[42] and enable the assessment of avalanche mobility based on initial ice or water content.

Methods

Seismic event clustering and volume estimation

We applied a self-supervised learning workflow[35] that combines representation learning with iterative clustering to identify and characterize slope-seismic activity preceding the 28 May 2025 collapse. At a high level, this algorithm relies on grouping signals with similar time-frequency characteristics, such as spectral distribution, signal envelope, and duration. This enables the model to distinguish impulsive signatures of discrete rockfalls from the emergent patterns of complex mass movements. The continuous vertical component (HHZ) waveform at station LAUCH, recorded between 1 January and 1 June 2025, was segmented into 180 s windows and converted into dual-panel images (spectrogram and high-pass filtered waveform > 1 Hz), yielding 73,387 images. A BYOL-based self-supervised model[75] encoded these images into 512-dimensional latent representations. The embeddings were first partitioned using k-means clustering (3000 centroids, 300 iterations) and then hierarchically merged based on an inconsistency coefficient of 3, resulting in 236 distinct signal clusters. Manual inspection and refined arrival-time picking yielded a high-confidence catalog of 2265 events, of which 17 clusters (≈ 700 events) showed clear pre-failure acceleration.

Event volumes were inferred from seismic energy and signal duration using the empirical scaling framework of refs. 30,31,37. Event durations were determined manually. For the seismic records, start and end times were picked based on the signal-to-noise ratio and spectrogram characteristics. For the SHALTOP simulations, similar to the approach by ref. 30, the end time was defined as the moment when no significant change was observed in the potential energy time series. Following the methodology of refs. 30,76, seismic energy was calculated by assuming a ground density of 2100 kg/m^3, a seismic wave velocity of 2500 m/s, a quality factor $Q = 100$, and a central frequency of 5 Hz.

To ensure realistic release dynamics in the SHALTOP simulations, the initial failure masses were reconstructed by distributing the predefined volumes across the source areas using a slope-weighted distribution. The volume assigned to each pixel was weighted inversely to the local terrain slope, allowing more mass to be allocated to flatter regions. The final basal failure surface was generated by subtracting these derived vertical depths from the pre-event DEM.

As introduced in the main text, the recorded seismic energy E_s is empirically linked to the loss of potential energy E_p[30]. Assuming proportionality between E_s and E_p via their respective power-law scalings with duration ($E_s = \alpha t_s^{\beta}$ and $E_p = \alpha\prime t_p^{\beta\prime}$ where $t_S = t_p$), we derived E_p from the energy conversion ratio $R_{ps} = \frac{E_p}{E_s}$, which is calibrated on the granular flow simulations (refer to Fig. 2c, d).

From the seismic recording, we can only measure the radiated seismic energy E_s. To relate E_s to the actual release volume (V_{real}), we rely on the relation $E_p = \rho gHV$, where ρ is the bulk density and H the mean fall height[30]. From the SHALTOP simulations, we extract both the explicitly known input volumes (V_{sim}) and their corresponding simulated kinematic potential energy ($E_{p,sim}$, which accounts for gHV) for the two families. Using these outputs, we establish a linear proportionality factor, R_{E_pV}, between $E_{p,sim}$ and V_{sim} by assuming a constant density ρ. By bridging the seismic observations and the granular flow simulations, we calculate the real event volume as $V_{real} \approx \frac{R_{ps}E_s}{R_{E_pV}}$.

We account for the substantial parameter uncertainties propagated through this approximation. Because the empirical power-law fits for E_s and E_p are not exactly with the same slope, the energy conversion ratio R_{ps} varies across the duration range. Furthermore, the source density ρ varies for each event. To establish a confidence envelope for the cumulative mass wasting volume, we calculated upper and lower volume bounds by varying these physical and empirical parameters. The energy ratio bounds ($R_{ps,min}$, $R_{ps,max}$) were extracted from the spread between the two fitted power-law lines for E_s and E_p. For Family 1 (rockfalls), we assumed a source mass density ρ from 2200 to 2700 kg m^{-3}, which reflects the variation between highly fractured rock mass and intact bedrock[77]. For Family 2 (small rock-ice avalanches), the source density also relies on the volumetric ice fraction. Treating these failures as binary mixtures of glacier ice and rock debris, we assumed an ice fraction variation between 30 and 70%. Using constituent densities of 917[78] for ice and 2667 kg m^{-3} for rock yields a ρ uncertainty range of 1009–1499 kg m^{-3} assuming a 0.7 solid fraction. By fitting a simple linear relation ($V_{sim} = a + b \cdot E_{p,sim}$) to the simulation outputs, we calculated specific conversion rates for each family. This generated a scaling coefficient (b) of 9.968×10^{-5} m^3/J for Family 1, and 1.066×10^{-4} m^3/J for Family 2. Finally, we convert the recorded seismic energy into potential energy using our calibrated conversion ratio ($E_p = E_s/R_{ps}$), and use this linear relation to estimate the real event volume: $V_{real} = a + b \cdot (E_s/R_{ps})$. The final upper and lower volume bounds were computed using the extreme combinations of R_{ps}, ρ, by the two boundaries.

Seismic force inversion and metrics calculation

We inverted the long-period (15–180 s) seismic waveforms from broadband stations between 33 and 110 km from the source to reconstruct the time-dependent center-of-mass force history. The point force was located at (46.40°, 7.84°). We omitted station LAUCH from the analysis because its close proximity to the event (5 km) violates the assumptions of the method. Other stations were omitted on a case-by-case basis if their data quality was clearly poor (e.g., excessive long-period noise). Data were detrended, tapered, corrected for instrument response to displacement (including a cosine taper filter with corners at 15 and 180 s), again detrended using a second-order spline to remove very-long-period artifacts, and again tapered. The inversion followed the *lsforce* approach[46,47] using the following parameters: `iasp91_2s` Earth model, no zero start imposition, no add-to-zero constraint, regularization parameter $\alpha = 1.5 \times 10^{-17}$, and Tikhonov ratios (0.4, 0, 0.6). Channels with remaining substantial very-long-period noise were down-weighted. The result achieves a variance reduction (VR) of 85%. Uncertainty was quantified via a jackknife scheme with 20 iterations, each dropping half of the input stations. VR ranged from 81 to 91% with a median of 86%, indicating stable solutions across station subsets. The seismically derived and numerical landslide model-derived forces were compared using four quantitative metrics: (1) deposit overlap (Trimline ratio), (2) deposit-thickness RMSE, (3) force cross-correlation, and (4) amplitude RMSE (refer to Supplementary Information S1 and Eqs. (S1)–(S4)).

Depth-averaged granular flow modeling

SHALTOP[39,79] solves the depth-averaged equations for dry granular flows on a complex topography[17,22,40–43]. The equations are depth-averaged along the direction normal to the topography to apply the shallow flow approximation accurately. Furthermore, SHALTOP accurately accounts for the complex topography curvature, which affects the dynamics and deposition of granular flows[43]. SHALTOP's strengths lie in the small number of parameters involved and its extensive validation through a series of laboratory experiments and field observations, including seismic data[16,21,28,29,39–42,64]. The model can handle different rheologies, including a Coulomb-type friction law with a constant or variable effective friction coefficient μ.

Simulations of dry landslides and rock avalanches show that the values of the friction coefficients in the models have to be very small to reproduce the runout distance and the dynamics of events with large volume[42,80]. These values are thus empirical. This increase of flow mobility with increasing volume remains an open key question. To obtain a first estimate of a typical friction coefficient with a volume $V \approx 9.3 \times 10^6\,\mathrm{m}^3$, we used the $\mu(V)$ law, where V is the avalanche volume, derived from numerical back-analyses of natural dry rock and debris avalanches using a constant Coulomb friction law[42]

$$\mu(V) = V^{-0.0774}. \tag{1}$$

Other tested laws include constant Coulomb, velocity-weakening[42], Voellmy, and rate-dependent $\mu(I)$ rheologies. For the main avalanche, best-fit parameters of $\mu(I)$ were $\mu_1 = 0.03$, $\mu_2 = 0.21$, $\varphi = 0.7$, $d = 0.5$ m, and $I_0 = 0.279$. Parameter sensitivity and full equations are given in Supplementary Information S2.

3D MPM granular flow modeling

To assess 3D effects, we conduct 3D continuum simulations of the rock-ice avalanche using MPM. This numerical method, typically attributed to ref. 81, allows for the capturing of solid-fluid transitions and naturally handles free surface dynamics. In an elasto-viscoplastic framework based on the multiplicative decomposition of the deformation gradient into an elastic and viscoplastic part, we formulate a Drucker–Prager model[82] which depends on the inertial number. As such, the $\mu(I)$-rheology can be recovered under flow conditions. For the main avalanche, best-fit parameters of $\mu(I)$ were $\mu_1 = 0.02$, $\mu_2 = 0.28$, $\varphi = 0.7$, $d = 0.3$ m, and $I_0 = 0.01$.

This versatile model enables the simulation of both cohesionless and cohesive granular flows, including snow, rock, or ice avalanches, as well as landslides. The details of the elasto-viscoplastic framework are comprehensively presented in refs. 52,83, which also introduces more advanced constitutive laws that may account for dilatancy and compressibility effects. Full constitutive details are provided in Supplementary Information S3. Following the framework of ref. 84, the 3D simulation results are in this article converted into depth-averaged variables for 2D visualization and metric evaluation.

Geotechnical field investigation

Four sediment samples were collected from the uppermost sediment layer of the deposits under the permission of the Canton of Valais, both on the counterslope and at the main deposit (Fig. 1b). Grain-size distribution (GSD) was determined on a weight basis using dry sieving, wet sieving, and hydrometer analysis to characterize the fraction finer than 16 mm, following the Swiss Norms[85]. The collected field samples also contained material coarser than 16 mm (coarse gravel and cobbles), which was proportionally scaled and included in the final GSD (Fig. 6a). Larger boulders were observed on site, but could not be incorporated into a complete GSD. Visual observations indicate (Supplementary Fig. S5), however, that these boulders are embedded within a matrix-supported mixture of cobbles, gravel, sand and fines. This indicates that landslide behavior was governed primarily by this sediment matrix rather than by interactions among boulders. Samples from the counterslope and the main deposit show similar GSDs, though the counterslope was visually richer in boulders, indicating preferential coarse deposition there while finer, more mobile fractions continued downstream.

Field-saturated hydraulic conductivity (K_{fs}) was measured in-situ at the south-western margin of the deposits (Fig. 1b) using the METER SATURO dual-head infiltrometer[86,87]. Three tests yielded relatively low values (average $K_{fs} = 1.5 \times 10^{-5}$ m/s) and high variability ($\sigma_{fs} = 1.5 \times 10^{-5}$ m/s). Nonetheless, a simple estimate of the saturated hydraulic conductivity using Hazen's empirical relation, based on mean $D_{10} = 0.033$ mm (the grain diameter at 10% passing, extracted from the measured GSDs), yielded a comparable value ($K_s = 1.1 \times 10^{-5}$ m/s), which is within the range of the SATURO measurements. Converting to intrinsic permeability using $k_0 = K_{fs}\eta_w\gamma_w^{-1}$, where γ_w is the unit weight of water and $\eta_w = 10^{-3}$ Pa · s its viscosity, gives $k_0 \approx 10^{-12}\,\mathrm{m}^2$.

Estimation of ice melt volume during the flow

To estimate the potential amount of ice melt generated by frictional and impact heating during the main avalanche, we computed an upper bound by first assuming that all potential energy released was converted into ice melt. The specific potential energy released per unit volume can be expressed as:

$$e_{\mathrm{pot}} = \rho_b g h, \tag{2}$$

where ρ_b is the bulk density of the mixture, $g = 9.81\,\mathrm{m\,s^{-2}}$, and h is the average fall height.

Assuming a mixture consisting of $\approx 3 \times 10^6\,\mathrm{m}^3$ of ice ($\rho_i = 917\,\mathrm{kg\,m^{-3}}$[78]) and $\approx 6.3 \times 10^6\,\mathrm{m}^3$ of rock ($\rho_r = 2667\,\mathrm{kg\,m^{-3}}$[77]), the bulk density is $\approx 2102\,\mathrm{kg\,m^{-3}}$. In addition, we should account for the porosity of the debris mass. Applying a typical solid fraction of 0.7 gives an effective density of $\approx 1472\,\mathrm{kg\,m^{-3}}$. The glacier was assumed to be temperate (i.e., at the pressure melting point), consistent with ice temperature measurements conducted 20 days after the collapse by the Laboratory of Hydraulics, Hydrology and Glaciology at ETH (unpublished data). Consequently, only the latent heat of fusion is considered in the energy balance.

Taking a mean fall height of $h \approx 1100$ m, the available specific potential energy is therefore $e_{\mathrm{pot}} \approx 1.58 \times 10^7\,\mathrm{J\,m^{-3}}$. The equivalent amount of ice melt per unit volume of mixture, assuming complete energy conversion, is:

$$m_{\mathrm{melt}} = \frac{e_{\mathrm{pot}}}{L} \approx 47.56\,\mathrm{kg\,m^{-3}}. \tag{3}$$

where $L = 3.34 \times 10^5\,\mathrm{J\,kg^{-1}}$ is the latent heat of fusion of ice[78]. In reality, the energy budget of a rock-ice avalanche is partitioned among multiple processes. For example, ref. 88 estimated fragmentation energies averaging about 20% of the potential energy for the studied rock avalanches. To account for these energy sinks, we assume a plausible range of energy conversion into ice heating of 20 to 50%. Applying this thermal efficiency to the available potential energy generates between 9.51 and 23.78 kg of meltwater per cubic meter. As a result, the dynamic frictional heating produces an estimated meltwater volume of $\approx 0.88 \times 10^5$ to $2.21 \times 10^5\,\mathrm{m}^3$.

Data availability

All seismic waveform data used in this study are publicly available from the Swiss Seismological Service (SED) at http://www.seismo.ethz.ch/en/knowledge/earthquake-data-and-analysis-tools/waveform-data/. The derived datasets, including geomorphological maps and geotechnical measurements, are available in a publicly accessible Zenodo repository on Zenodo under https://doi.org/10.5281/zenodo.21511788 Kang et al.[89]. The original high-resolution digital elevation models are owned by the Municipality of Blatten and currently cannot be publicly redistributed.

Code availability

Codes used for post-processing, model evaluation, and figure generation is openly available on Zenodo under https://doi.org/10.5281/zenodo.21511788 Kang et al.[89]. The self-supervised seismic clustering algorithm is available on GitLab at https://gitlab.com/eost/seis-clust-ssl. The *lsforce* inversion code can be accessed at https://code.usgs.gov/ghsc/lhp/lsforce, the SHALTOP model at https://zenodo.org/records/10964107, and the Matter framework at https://github.com/larsblatny/matter/.

Received: 6 March 2026; Accepted: 18 August 2026;
Published online: 07 September 2026

References

1. Shugar, D. H. et al. A massive rock and ice avalanche caused the 2021 disaster at Chamoli, Indian Himalaya. *Science* **373**, 300–306 https://doi.org/10.1126/science.abh4455 (2021).
2. Svennevig, K. et al. A rockslide-generated tsunami in a Greenland fjord rang earth for 9 days. *Science* **385**, 1196–1205 https://doi.org/10.1126/science.adm9247 (2024).
3. Yanites, B. J. et al. Cascading land surface hazards as a nexus in the Earth system. *Science* **388**, eadp9559 https://doi.org/10.1126/science.adp9559 (2025).
4. Cook, K. L. et al. Detection and potential early warning of catastrophic flow events with regional seismic networks. *Science* **374**, 87–92 https://doi.org/10.1126/science.abj1227 (2021).
5. Li, G. et al. Connectivity of earthquake-triggered landslides with the fluvial network: implications for landslide sediment transport after the 2008 Wenchuan earthquake. *J. Geophys. Res.: Earth Surf.* **121**, 703–724 https://doi.org/10.1002/2015JF003718 (2016).
6. Kääb, A. et al. Sudden large-volume detachments of low-angle mountain glaciers – more frequent than thought? *Cryosphere* **15**, 1751–1785 (2021).
7. Jacquemart, M. et al. Detecting the impact of climate change on alpine mass movements in observational records from the European Alps. *Earth-Sci. Rev.* **258**, 104886 (2024).
8. Shugar, D. H. et al. A 481-meter-high landslide-tsunami in a cruise ship-frequented Alaska fjord. *Science* eaec3187 https://doi.org/10.1126/science.aec3187 (2026).
9. Li, Y. et al. Glacier retreat in eastern Himalaya drives catastrophic glacier hazard chain. *Geophys. Res. Lett.* **51**, e2024GL108202 https://doi.org/10.1029/2024GL108202 (2024).
10. Federal Office for the Environment (FOEN/BAFU). *Natural Hazards: In brief (2024)*. (Accessed 10 September 2025) https://www.bafu.admin.ch/bafu/en/home/topics/natural-hazards/in-brief.html.
11. Petley, D. *The 28 April 2025 Glacial Outburst Flood (GLOF)/Landslide at Vallunaraju in Peru* https://eos.org/thelandslideblog/vallunaraju-1 (2025).
12. Poli, P. Creep and slip: seismic precursors to the Nuugaatsiaq landslide (Greenland). *Geophys. Res. Lett.* **44**, 8832–8836 https://doi.org/10.1002/2017GL075039 (2017).
13. Lacroix, P., Biévre, G., Pathier, E., Kniess, U. & Jongmans, D. Use of Sentinel-2 images for the detection of precursory motions before landslide failures. *Remote Sens. Environ.* **215**, 507–516 (2018).
14. Paitz, P. et al. Phenomenology of avalanche recordings from distributed acoustic sensing. *J. Geophys. Res.: Earth Surf.* **128**, e2022JF007011 https://doi.org/10.1029/2022JF007011 (2023).
15. Kang, J. et al. Automatic monitoring of rock-slope failures using distributed acoustic sensing and semi-supervised learning. *Geophys. Res. Lett.* **51**, e2024GL110672 https://doi.org/10.1029/2024GL110672 (2024).
16. Favreau, P., Mangeney, A., Lucas, A., Crosta, G. & Bouchut, F. Numerical modeling of landquakes. *Geophys. Res. Lett.* **37**, L15305 (2010).
17. Peruzzetto, M. et al. Simplified simulation of rock avalanches and subsequent debris flows with a single thin-layer model: application to the Prêcheur river (Martinique, Lesser Antilles). *Eng. Geol.* **296**, 106457 (2022).
18. Hungr, O. Entrainment of debris in rock avalanches: an analysis of a long run-out mechanism. *GSA Bull.* **116**, 1240–1252 (2004).
19. Iverson, R. et al. Landslide mobility and hazards: implications of the 2014 Oso disaster. *Earth Planet. Sci. Lett.* **412**, 197–208 (2015).
20. McDougall, S. 2014 Canadian Geotechnical Colloquium: landslide runout analysis - current practice and challenges. *Can. Geotech. J.* **54**, 605–620 https://doi.org/10.1139/cgj-2016-0104 (2017).
21. Moretti, L. et al. Constraining landslide characteristics with Bayesian inversion of field and seismic data. *Geophys. J. Int.* **221**, 1341–1348 (2020).
22. Moretti, L., Mangeney, A., Capdeville, Y., Stutzmann, E. & Bouchut, F. Numerical modeling of the Mount Steller landslide flow history and of the generated long-period seismic waves. *Geophys. Res. Lett.* **39**, L16402 (2012).
23. Ekström, G. & Stark, C. P. Simple scaling of catastrophic landslide dynamics. *Science* **339**, 1416–1419 (2013).
24. Allstadt, K. Extracting source characteristics and dynamics of the August 2010 Mount Meager landslide from broadband seismograms. *J. Geophys. Res.: Earth Surf.* **118**, 1472–1490 https://doi.org/10.1002/jgrf.20110 (2013).
25. Hibert, C., Ekström, G. & Stark, C. P. Dynamics of the Bingham Canyon mine landslides from seismic signal analysis. *Geophys. Res. Lett.* **41**, 4535–4541 (2014).
26. Walter, F. et al. Direct observations of a three million cubic meter rock-slope collapse with almost immediate initiation of ensuing debris flows. *Geomorphology* **351**, 106933 (2020).
27. Svennevig, K. et al. A rockslide-generated tsunami in a Greenland fjord rang earth for 9 days. *Science* **385**, 1196–1205 (2024).
28. Yamada, M., Mangeney, A., Matsushi, Y. & Moretti, L. Estimation of dynamic friction of the Akatani landslide from seismic waveform inversion and numerical simulation. *Geophys. J. Int.* **206**, 1479–1486 (2016).
29. Moretti, L., Mangeney, A., Allstadt, K., Capdeville, Y. & Stutzmann, E. Numerical modeling of the Mount Meager landslide constrained by its force history derived from seismic data. *J. Geophys. Res.: Solid Earth* **120**, 2579–2599 (2015).
30. Hibert, C., Mangeney, A., Grandjean, G. & Shapiro, N. M. Slope instabilities in Dolomieu crater, Réunion island: from seismic signals to rockfall characteristics. *J. Geophys. Res.: Earth Surf.* **116**, F04032 (2011).
31. Levy, C. et al. Friction weakening in granular flows deduced from seismic records at the soufriére hills volcano, Montserrat. *J. Geophys. Res.: Solid Earth* **120**, 7536–7557 https://doi.org/10.1002/2015JB012151 (2015).
32. Farinotti, D. et al. *Fact Sheet for the Now-Collapsed Birchgletscher, Switzerland*. Tech. Rep. 88028-VAW-2025-07 (ETH Zurich Laboratory of Hydraulics, Hydrology and Glaciology VAW, and Swiss Federal Institute for Forest, Snow and Landscape Research (WSL), Zurich, 2025).
33. SRF News. Lonza steigt +++ gampel/steg sollen sich auf Räumung vorbereiten https://www.srf.ch/news/schweiz/dorf-blatten-verschuettet-lonza-steigt-gampel-steg-sollen-sich-auf-raeumung-vorbereiten (2025).
34. Swiss Seismological Service. Mass movements http://www.seismo.ethz.ch/en/earthquakes/switzerland/massmovements/ (2025).
35. Rimpot, J., Hibert, C., Malet, J.-P., Forestier, G. & Weber, J. Self-supervised learning based clustering workflow for exploring seismological data from dense networks. *J. Geophys. Res.: Mach. Learn. Comput.* **2**, e2025JH000958 https://doi.org/10.1029/2025JH000958 (2025).
36. Durand, V. et al. Repetitive small seismicity coupled with rainfall can trigger large slope instabilities on metastable volcanic edifices. *Commun. Earth Environ.* **4**, 383 https://doi.org/10.1038/s43247-023-00996-y (2023).
37. Farin, M., Mangeney, A., de Rosny, J., Toussaint, R. & Trinh, P.-T. Link between the dynamics of granular flows and the generated seismic signal: insights from laboratory experiments. *J. Geophys. Res.: Earth Surf.* **123**, 1407–1429 https://doi.org/10.1029/2017JF004296 (2018).
38. Mangeney-Castelnau, A. et al. Numerical modeling of avalanches based on Saint-Venant equations using a kinetic scheme. *J. Geophys. Res.: Solid Earth* **108**, 2527 (2003).

39. Mangeney-Castelnau, A. et al. On the use of Saint Venant equations to simulate the spreading of a granular mass: numerical simulation of granular spreading. *J. Geophys. Res.: Solid Earth* **110**, B09103 (2005).
40. Lucas, A. & Mangeney, A. Mobility and topographic effects for large Valles Marineris landslides on Mars. *Geophys. Res. Lett.* **34**, L10201 (2007).
41. Lucas, A., Mangeney, A., Mège, D. & Bouchut, F. Influence of the scar geometry on landslide dynamics and deposits: application to Martian landslides. *J. Geophys. Res.* **116**, E10 (2011).
42. Lucas, A., Mangeney, A. & Ampuero, J. P. Frictional velocity-weakening in landslides on Earth and on other planetary bodies. *Nat. Commun.* **5**, 3417 https://doi.org/10.1038/ncomms4417 (2014).
43. Peruzzetto, M. et al. Topography curvature effects in thin-layer models for gravity-driven flows without bed erosion. *J. Geophys. Res.: Earth Surf.* **126**, e2020JF005657 (2021).
44. MeteoSwiss. *Hourly Precipitation Data From Automatic Weather Stations* (Federal Office of Meteorology and Climatology, accessed October 2025, 2025).
45. Zhou, G. G. D. et al. Segregation-induced flow transitions in rock-ice mixtures: implications for rock-ice avalanche dynamics. *J. Geophys. Res.: Earth Surf.* **129**, e2024JF007831 https://doi.org/10.1029/2024JF007831 (2024).
46. Toney, L. & Allstadt, K. E. lsforce: a Python-based single-force seismic inversion framework for massive landslides. *Seismol. Res. Lett.* **92**, 2610–2626 https://doi.org/10.1785/0220210004 (2021).
47. Allstadt, K. E., Toney, L. & Collins, E. A. *lsforce (Version 1.1) [Source Code]* (U.S. Geological Survey (USGS), 2023).
48. Kawakatsu, H. Centroid single force inversion of seismic waves generated by landslides. *J. Geophys. Res.: Solid Earth* **94**, 12363–12374 https://doi.org/10.1029/JB094iB09p12363 (1989).
49. Hibert, C., Stark, C. P. & Ekström, G. Dynamics of the oso-steelhead landslide from broadband seismic analysis. *Nat. Hazards Earth Syst. Sci.* **15**, 1265–1273 (2015).
50. Hibert, C., Ekström, G. & Stark, C. P. The relationship between bulk-mass momentum and short-period seismic radiation in catastrophic landslides. *J. Geophys. Res.: Earth Surf.* **122**, 1201–1215 https://doi.org/10.1002/2016JF004027 (2017).
51. Gaume, J., Gast, T., Teran, J., van Herwijnen, A. & Jiang, C. Dynamic anticrack propagation in snow. *Nat. Commun.* **9**, 3047 https://doi.org/10.1038/s41467-018-05181-w (2018).
52. Blatny, L., Gray, J. & Gaume, J. A critical state μ(i)-rheology model for cohesive granular flows. *J. Fluid Mech.* **997**, A67 (2024).
53. Federal Office of Topography swisstopo. *Rapid Mapping* https://www.rapidmapping.admin.ch/index_de.html (2025).
54. Kreyszig, E. *Advanced Engineering Mathematics* 4th edn (Wiley, New York, 1979).
55. Jop, P., Forterre, Y. & Pouliquen, O. A constitutive law for dense granular flows. *Nature* **441**, 727–730 (2006).
56. Iverson, R. M. & George, D. L. A depth-averaged debris-flow model that includes the effects of evolving dilatancy. I. Physical basis. *Proc. R. Soc. A: Math. Phys. Eng. Sci.* **470**, 20130819 (2014).
57. Iverson, R. M. & George, D. L. Modelling landslide liquefaction, mobility bifurcation and the dynamics of the 2014 Oso disaster. *Geotechnique* **66**, 175–187 (2016).
58. Bouchut, F., Ferná ndez-Nieto, E. D., Mangeney, A. & Narbona-Reina, G. A two-phase two-layer model for fluidized granular flows with dilatancy effects. *J. Fluid Mech.* **801**, 166–221 (2016).
59. Munch, J., Zhuang, Y., Dash, R. K. & Bartelt, P. Dynamic thermomechanical modeling of rock-ice avalanches: understanding flow transitions, water dynamics, and uncertainties. *J. Geophys. Res.: Earth Surf.* **129**, e2024JF007805 https://doi.org/10.1029/2024JF007805 (2024).
60. Vicari, H., Tran, Q.-A., Metzsch Juel, M. & Gaume, J. The role of dilatancy and permeability of erodible wet bed sediments in affecting erosion and runout of a granular flow: two-phase MPM–CFD simulations. *Comput. Geotech.* **185**, 107307 (2025).
61. Bouchut, F., Drach, E., Fernández-Nieto, E. D., Mangeney, A. & Narbona-Reina, G. A series of two-phase models for grain–fluid flows with dilatancy. *J. Fluid Mech.* **1008**, A43 (2025).
62. Schneider, D., Huggel, C., Haeberli, W. & Kaitna, R. Unraveling driving factors for large rock-ice avalanche mobility. *Earth Surf. Process. Landf.* **36**, 1948–1966 https://doi.org/10.1002/esp.2218 (2011).
63. Cappa, F., Guglielmi, Y., Viseur, S. & Garambois, S. Deep fluids can facilitate rupture of slow-moving giant landslides as a result of stress transfer and frictional weakening. *Geophys. Res. Lett.* **41**, 61–66 https://doi.org/10.1002/2013GL058566 (2014).
64. Yamada, M., Mangeney, A., Matsushi, Y. & Matsuzawa, T. Estimation of dynamic friction and movement history of large landslides. *Landslides* **15**, 1963–1974 (2018).
65. Wang, C., Cui, Y., Song, D., Nie, J. & Hu, B. Effect of ice content on the interaction between rock-ice avalanche and rigid barrier: physical and numerical modelling. *Comput. Geotech.* **150**, 104924 (2022).
66. Fan, X. et al. The friction behavior of rock-ice avalanches in relation to rock-ice segregation: insights from flume physical experiments. *J. Geophys. Res.: Earth Surf.* **130**, e2024JF007904 (2025).
67. Feng, Z. et al. How ice particles increase mobility of rock-ice avalanches: insights from chute flows simulation of granular rock-ice mixtures by discrete element method. *J. Geophys. Res.: Earth Surf.* **128**, e2023JF007115 (2023).
68. Bowman, E., Take, W., Rait, K. & Hann, C. Physical models of rock avalanche spreading behaviour with dynamic fragmentation. *Can. Geotech. J.* **49**, 460–476 https://doi.org/10.1139/t2012-007 (2012).
69. Sosio, R., Crosta, G. B., Chen, J. H. & Hungr, O. Modelling rock avalanche propagation onto glaciers. *Quat. Sci. Rev.* **47**, 23–40 (2012).
70. Iverson, R. M. The physics of debris flows. *Rev. Geophys.* **35**, 245–296 (1997).
71. Jacquemart, M. et al. Geomorphic and sedimentary signatures of catastrophic glacier detachments: a first assessment from Flat Creek, Alaska. *Geomorphology* **414**, 108376 (2022).
72. Coe, J. A., Bessette-Kirton, E. K. & Geertsema, M. Increasing rock-avalanche size and mobility in Glacier Bay National Park and Preserve, Alaska detected from 1984 to 2016 Landsat imagery. *Landslides* **15**, 393–407 https://doi.org/10.1007/s10346-017-0879-7 (2018).
73. Kristensen, L. et al. Movements, failure and climatic control of the Veslemannen rockslide, Western Norway. *Landslides* **18**, 1963–1980 https://doi.org/10.1007/s10346-020-01609-x (2021).
74. Schneider, D. et al. Insights into rock-ice avalanche dynamics by combined analysis of seismic recordings and a numerical avalanche model. *J. Geophys. Res.: Earth Surf.* **115** https://doi.org/10.1029/2010JF001734 (2010).
75. Grill, J. et al. Bootstrap your own latent: a new approach to self-supervised learning. 14 (Curran Associates Inc., 2020).
76. Vilajosana, I. et al. Rockfall induced seismic signals: case study in Montserrat, Catalonia. *Nat. Hazards Earth Syst. Sci.* **8**, 805–812 (2008).
77. Daly, R. A., Manger, G. E., Clark, J. & Sydney, P. Section 4: density of rocks. In *Handbook of Physical Constants* (ed. Sydney P. Clark, Jr.) (Geological Society of America, Boulder, CO, 1966).
78. Cuffey, K. M. & Paterson, W. S. B. *The Physics of Glaciers* 4th edn (Elsevier, Oxford, UK, 2010).
79. Bouchut, F., Mangeney-Castelnau, A., Perthame, B. & Vilotte, J.-P. A new model of Saint Venant and Savage–Hutter type for gravity driven shallow water flows. *Comptes Rendus Math.* **336**, 531–536 (2003).
80. Delannay, R., Valance, A., Mangeney, A., Roche, O. & Richard, P. Granular and particle-laden flows: from laboratory experiments to field observations. *J. Phys. D: Appl. Phys.* **50**, 053001 https://doi.org/10.1088/1361-6463/50/5/053001 (2017).

81. Sulsky, D., Chen, Z. & Schreyer, H. L. A particle method for history-dependent materials. *Comput. Methods Appl. Mech. Eng.* **118**, 179–196 (1994).
82. Drucker, D. C. & Prager, W. Soil mechanics and plastic analysis for limit design. *Q. Appl. Math.* **10**, 157–165 (1952).
83. Blatny, L. & Gaume, J. Matter (v1): an open-source MPM solver for granular matter. *EGUsphere* **2025**, 1–29 (2025).
84. Vicari, H., Kyburz, M. L. & Gaume, J. Brief communication: depth-averaging of 3D depth-resolved MPM simulation results of geophysical flows for GIS visualization. *Nat. Hazards Earth Syst. Sci.* **25**, 3897–3904 (2025).
85. SN EN ISO 17892-4:2018-12. *Geotechnische Erkundung und Untersuchung, Laborversuch an Bodenproben – Teil 4: Bestimmung der Korngrössenverteilung* (Swiss Association of Road and Transportation Experts (VSS), 2018).
86. ASTM D8550-25. *Standard Test Method for Determination of Infiltration Rate and Calculating Field Hydraulic Conductivity of Field Soils by Sealed Single-Ring Infiltrometer and Multiple Pressure Head Procedure* (ASTM International, 2025).
87. Vicari, H. et al. Linking debris flow erosion to channel-bed parameters: geotechnical and UAS-based investigation of ten channels in Switzerland. *Geomorphology* **509**, 110360 (2026).
88. Locat, P., Couture, R., Leroueil, S., Locat, J. & Jaboyedoff, M. Fragmentation energy in rock avalanches. *Can. Geotech. J.* **43**, 830–851 https://doi.org/10.1139/t06-045 (2006).
89. Kang, J. et al. Simulation data and scripts for Blatten rock-ice avalanche https://doi.org/10.5281/zenodo.21511788 (2026).
90. Federal Office of Topography swisstopo. Swissimage 10 cm https://www.swisstopo.admin.ch/en/orthoimage-swissimage-10 (2024).
91. Federal Office of Topography swisstopo. swissalti3d https://www.swisstopo.admin.ch/en/height-model-swissalti3d (2024).

Acknowledgements
Authors are grateful to Ralf Herzog (ETHZ) for performing grain size distribution analysis of Blatten sediments, and thank the Albert Lück-Stiftung for their financial support. We thank Simeon Schmauß for sharing the publicly accessible DEM reconstruction used in our initial tests. We gratefully acknowledge the constructive feedback provided by Katy Barnhart during the U.S. Geological Survey (USGS) internal review process, which significantly improved the quality of this manuscript. Any use of trade, firm, or product names is for descriptive purposes only and does not imply endorsement by the U.S. Government.

Author contributions
Conceptualization: J.K., A.L., F.W., A.M., J.G., K.A., C.H., L.T., M.D. Data curation: J.K., F.W., J.G., H.V., M.J., D.F., A.L., K.A., C.H., L.T., Data Investigation: J.K., A.L., A.M., J.G., K.A., C.H., L.T., H.V., M.D., M.J. Software: A.M., J.G., A.L., K.A., C.H., L.T., J.K., M.P., L.B., M.L.K., J.R., Supervision: F.W., A.L., A.M., J.G. Validation: J.K., A.L., A.M., J.G., K.A., C.H., L.T., H.V., M.J. Visualization: J.K., A.L., J.G., K.A., C.H., L.T., H.V., M.J. Writing–original draft: J.K., A.L., A.M., J.G., F.W., H.V., C.H., M.J., L.B.

Funding
J.K., F.W., and A.M. have received funding from the European Union's Horizon 2021 research and innovation program (EnvSeis) under grant agreement No. 101073148. A.L. acknowledges support from CNES for the STERREO project. L.B. acknowledges support from the Swiss National Science Foundation (grant number P500PT_230265). C.H. and J.R. have received funding by the Agence Nationale de la Recherche (ANR) - Projet ANR-20-CE01-0006 "HighLand: Landslides and Climate Change in highly Sensible Environments: Seismology, Earth Observation and Artificial Intelligence." Open Access funding provided by Lib4RI – Library for the Research Institutes within the ETH Domain: Eawag, Empa, PSI & WSL.

Competing interests
The authors declare no competing interests.

Additional information
Supplementary information The online version contains supplementary material available at https://doi.org/10.1038/s43247-026-03983-1.

Correspondence and requests for materials should be addressed to Jiahui Kang or Fabian Walter.

Peer review information *Communications Earth & Environment* thanks Wangcheng Zhang and the other, anonymous, reviewer(s) for their contribution to the peer review of this work. Primary Handling Editors: Joe Aslin. A peer review file is available.